scientific reports

Check for updates

OPEN

Hierarchical sparse Bayesian learning with adaptive Laplacian prior for single image super-resolution

Mingming Qi[1,2], Yue Zhou[3], Yiwei Hu[4], Cuihua Xie[5] & Shuhua Xu[1,2]✉

Single-image super-resolution (SISR) continues to face difficulties in reconstructing perceptually critical details from degraded low-resolution observations. While conventional Bayesian approaches utilizing Relevance Vector Machines (RVMs) provide probabilistic interpretations, their reliance on fixed blur kernel definitions and homogeneous pixel dependency models often yields artifacts in complex scenarios. To resolve these issues, this study introduces a hierarchical Bayesian architecture enhanced by an adaptive Laplacian prior, which extends the sparse Bayesian learning (SBL) paradigm. Diverging from traditional Gaussian-based frameworks, our method employs sparsity-inducing regularization to selectively prioritize structurally salient regions (e.g., edge discontinuities, texture boundaries), while dynamically quantifying reconstruction uncertainty through pixel-wise variance analysis. Additionally, a spatially adaptive optimization mechanism is designed to streamline computational workflows without compromising restoration fidelity. Evaluations across multiple benchmarks confirm the framework's advantages: it surpasses existing state-of-the-art techniques in both quantitative metrics (PSNR, SSIM) and qualitative assessments, demonstrating superior artifact suppression in high-frequency domains. Comparative analyses against recent state-of-the-art models further validate its capability to harmonize sparse representation with structural coherence.

Keywords Single image super-resolution (SISR), Sparse bayesian learning (SBL), Adaptive laplacian prior, Hierarchical bayesian model, Pixel variance estimation, Spatial alternating optimization

SISR represents a classical research topic within the field of computer vision, which has garnered significant attention in recent years. The objective of this research is to reconstruct HR images from their LR counterparts[1]. HR images are crucial in various applications, including biometric recognition, medical imaging, satellite remote sensing, billboard monitors, guidance technology, optical-electric measurement, and advanced interactive interfaces[2]. While extensive research has been conducted on SISR methodologies over the past few decades, research on efficient SR methodologies remains challenging due to issues such as blurring (geometric transformation), deformation, interpolation parameters, and noise-induced detail blurring[3]. Current SISR techniques exhibit three principal constraints: First, non-blind algorithms depend on precise blur kernel specifications, whereas blind techniques demonstrate limited generalization capability when handling intricate degradation patterns[4,5]. Second, predetermined sparse priors such as Gaussian distributions[6] show insufficient flexibility for varying texture characteristics. Third, Bayesian frameworks continue to encounter efficiency challenges in computational implementation[7–9].

Recently, a growing contingent of scholars have turned their attention to SISR based on sparse representation. Essentially, SISR can be categorized into three types: non-blind SR approaches, blind SR approaches, and learning-based algorithms. Blind SR techniques operate under the premise that both HR images and blur kernels are unknown, whereas non-blind techniques presuppose that only HR images are unknown, with the blur kernel being known. Non-blind SR methods can effectively enhance LR images affected by various blur kernels without the need for training, thus yielding superior SR results. However, in natural images, the blur kernel is often unknown or challenging to align with the ideal blur kernel assumption, thus constraining the

[1]School of Data Science and Artificial Intelligence, Wenzhou University of Technology, Wenzhou 325000, China. [2]Key Laboratory of Data Intelligence and Governance of Wenzhou City, Wenzhou 325000, China. [3]Wenzhou Federation of Trade Unions Workers' Technical Cooperation Center, Wenzhou 325000, China. [4]College of Computer Science and Artificial Intelligence, Wenzhou University, Wenzhou 325000, China. [5]School of Economics and Management, Wenzhou University of Technology, Wenzhou 325000, China. ✉email: 247141328@qq.com

applicability of this approach. Blind SR methods exhibit robust generalizability for SISR tasks, as they analyze the mapping rules from LR to HR images across numerous training samples[4,5]. Under this assumption, both the training and test sample sets share identical blur kernels, implying that the learning outcomes from the training datasets are transferable to the test datasets. Currently, machine learning methodologies are frequently utilized in SISR algorithms for the processes of learning and inference. Nevertheless, many of these methods primarily concentrate on image deconvolution and are heavily reliant on the choice of blur kernel, resulting in their limited adaptability, implying that SR processing methods may produce varied effects on different LR images.

Interpolation-based image SR is a classic technique known for its simplicity and ease of implementation. It employs various interpolation kernels to predict the values of missing pixels in HR images. Conventional interpolation methods encompass linear, nearest neighbor, and bicubic interpolation. However, given that these kernels usually exhibit isotropic, they fail to fully account for the anisotropic characteristics of complex image structures. This can lead to blurring effects and the loss of high-frequency details, especially at elevated magnification ratios. To address this limitation, researchers have proposed anisotropic interpolation algorithms capable of adapting to the inherent structure of images. While interpolation-based algorithms offer speed and simplicity, they are susceptible to blurring or jagged artifacts.

Learning-based algorithms are commonly employed to establish the mapping relationship from LR to HR image blocks by leveraging prior information derived from external pairs of LR and HR image blocks. While these algorithms are highly effective in reconstructing image details, the absence of non-local spatial and structural redundancy leads to the loss of certain high-frequency information, which in turn causes the reconstructed details to appear blurred. The sparse coding-based SR algorithm introduced by Yang et al.[10] represents a seminal learning-based approach, with numerous extensions reported in the literature. The learning-based reconstruction algorithm addresses the inverse SR problem by incorporating specific prior information into the target HR image. Broadly speaking, these methods can be elucidated from the probabilistic standpoint within one Bayesian maximum a posteriori (MAP) framework. Common prior distributions comprise total variation, bilateral constraints, edge-oriented assumptions, and non-local priors. Motivated by the remarkable achievements of deep learning, convolutional neural networks (CNNs) have recently been employed for image SR, leading to substantial enhancements in precision. Dong et al.[11] introduced the SR convolutional neural network (SRCNN) and showed that CNNs are capable of effectively learning the transformation from LR to HR image blocks in a seamless end-to-end fashion. Nonetheless, the prior information within SRCNN is derived from training data, often neglecting domain expertise crucial for tackling SR problems. Additionally, these algorithms typically demand significant computational resources.

Utilizing prior knowledge of images can significantly improve image reconstruction performance[12]. Nevertheless, accurately acquiring this prioritized knowledge remains challenging, thereby limiting the enhancement of reconstruction performance. Recent advances in sparse prior modeling further demonstrate the importance of adaptive regularization. Recent work by Yang et al.[6] demonstrates that hybrid Gaussian priors can enhance sparse coding flexibility.

Over the past decade, driven by the rapid advancement of compressed sensing techniques, sparse recovery theory has exhibited significant promise, particularly in the realm of image reconstruction. Jiang and Wang et al.[13,14] introduced one SR method founded on sparse recovery, which successfully produced HR images. This algorithm exploits the property that images can be expressed as sparse linear combinations using overcomplete dictionaries[15]. Utilizing the sparse representation coefficients calculated from image blocks in LR image as those for HR image results in good reconstruction performance. Yan etal[16]. exploited the symmetry inherent in the uniform linear array of images to obtain more precise estimates via reconstruction techniques. LASSO is commonly employed in modeling image reconstruction problems, employing L1 regularization for feature selection to minimize model complexity[17,18]. Nevertheless, choosing regularization coefficients poses a challenge. A large regularization coefficient leads to model underfitting, while a small one fails to impose adequate constraints on the model, thus violating the Oracle property. Zou et al.[19] introduced the adaptive LASSO to exploit Oracle properties[20]. The adaptive LASSO allocates weights adaptively according to various L1 regularization parameters or coefficients, instead of relying on a single universal regularization parameter. While these SR methods can deliver satisfactory reconstruction quality, the ambiguity of blur degradation factors in LR images makes selecting regularization parameters quite challenging[21]. Poor parameter selection may lead to false peaks beyond the clutter ridge[22]significantly reducing the precision of sparse recovery, thereby impacting the effectiveness of noise blur removal and reconstruction[23]. Hence, addressing the three factors that impact image quality—noise, blur, and downsampling—is crucial when utilizing these algorithms[24–28]. Sparse Bayesian learning offers a resilient reconstruction algorithm for addressing sparse signal recovery issues, with all parameters being adaptively adjusted throughout the learning process. Tipping proposed SBL in 2001[29]. This marked the first application of an expectation maximization (EM)-based SBL strategy with forward-backward multiple measurement distances to HR imaging, termed EM-SBL-SR[7]. Li et al.[8] employed a non-parametric sparse Bayesian dictionary learning algorithm to improve the spatial resolution of remote sensing imagery. Wan et al.[9] proposed one robust and rapidly converging sparse Bayesian learning method to enhance convergence. Viewed through a Bayesian lens, the previously mentioned LASSO problem can be framed as estimating MAP under one Laplace prior[30]. Additionally, the Laplace prior distribution exhibits a sharper peak and slightly thicker tails compared to the Gaussian distribution, thereby promoting sparsity. However, due to the Laplace distribution's lack of conjugacy with the Gaussian distribution, describing the posterior distribution becomes challenging when directly employing the Laplace prior to modeling complex signals. Consequently, Chaabene et al.[31] proposed one hierarchical Bayesian framework to derive the Laplace prior for the true signal value. Natural image sparsity can be more effectively modeled using adaptive Laplacian distributions rather than Gaussian priors[6,30]since their extended tail behavior preserves edge features while concentrated peaks attenuate noise interference. The inherent non-conjugacy between Laplace priors and Gaussian likelihoods[31] necessitates an

alternative approach. Our solution introduces a hierarchical architecture that independently governs sparsity parameters and regularization intensity, facilitating concurrent optimization of reconstruction fidelity and adaptive performance. Therefore, in this article, we present a SISR method utilizing adaptive Laplacian prior sparse Bayesian estimation that jointly optimizes sparsity and regularization strength, enabling edge-aware recovery without kernel assumptions and delineate its contributions:

(1) In the reconstruction of SISR, we employ an adaptive Laplacian prior to enhance sparsity to a greater degree.
(2) We introduce hierarchical sparse Bayesian estimation into SISR reconstruction to enable adaptive adjustment of all parameters throughout the estimation process, thus enhancing the robustness of the algorithm.
(3) By tackling primary bottlenecks like covariance matrix storage and inverse operations, we successfully alleviated the computational load of the reconstruction technique.

The rest of our article is as outlined below: The section"SISR reconstruction model and SBL-SR reconstruction model"will elaborate on the SR model and SBL-SR model; the section"The proposed algorithm"will describe the algorithm proposed in our article; the section"Experimental results"will showcase the experimental outcomes and assess the quality of the reconstructed images; and the concluding section will summarize the findings.

SISR reconstruction model and SBL-SR reconstruction model

This study investigates the SR problem (ALP-SBL-SR) utilizing sparse Bayesian learning with adaptive Laplacian prior (ALP-SBL), offering a novel approach to enhancing the quality of reconstructed images. Thus, this section initially delineates the SISR reconstruction model and the SBL-SR reconstruction model.

SISR reconstruction model

The goal of SISR reconstruction is to reconstruct the corresponding HR image from its LR counterpart. Typically, a LR image, denoted as $y_i \in \mathbb{R}^{c\times d}$, is regarded as the result of processing a HR image $x_i \in \mathbb{R}^{c\times d}$, through a degraded model, i.e., $y_i = D(x_i;\delta)$. Here, D represents the degraded model, x_i represents the corresponding HR image, and δ represents parameters in the degraded model, such as sampling multiples, noise levels, or the parameters of the blur effect. In reality, the process of image degradation is uncertain and challenging to predict due to potential effects from various degradation processes like artifacts, distortions, noise, and blurring. To better emulate real-world scenarios, the degradation process is often modeled as a combination of multiple degradation models, namely

$$y_i = D(x_i;\delta) = (x_i \otimes k)\downarrow s + n_\zeta = \Phi A + n_\zeta, \{k, s, \zeta\} \subset \delta \tag{1}$$

where, $x_i \otimes k$ denotes the convolution of one HR image $\mathrm{x_i}$ with the blur kernel k. The term n_ζ signifies the presence of additive Gaussian white noise with one standard deviation value ζ. The symbol $\Phi = [x_1, x_2, \cdots, x_J] \in \mathbb{R}^{d\times J}$ denotes the overcomplete dictionary, with J denoting its number of elements. Lastly, $A \in \mathbb{R}^{J\times M}$ represents the contour matrix, where each nonzero column signifies a potential data component and M represents the number of input data points.

In compressed sensing, if one signal $X \in \mathbb{R}^{c\times d}$ is sparse, there exists a transform basis $\Psi \in \mathbb{R}^{cd\times J}$ such that the signal can be represented in the domain Ψ by Eq. (2):

$$X = \Psi A \tag{2}$$

where, A represents a $J \times M$-dimensional sparse coefficient, indicating that most of its values are zero.

Design an observation matrix $f \in \mathbb{R}^{cd\times cd}$, and compute the observation value $y_i\,(i = 1,2,\cdots,M)$ by taking the inner product of the cd row vectors in f with signal X, considering the noise n_ζ introduced during the observation process. The resulting observation value is denoted as $Y = (\mathrm{y_1}, \mathrm{y_2}, \cdots, \mathrm{y_M})^{\mathrm{T}}$, then,

$$Y = fX + \mathrm{n} \tag{3}$$

Substituting Eq. (2) into Eq. (3) results in

$$Y = \Phi A + n_\zeta, \text{ and } \Phi = f\Psi \tag{4}$$

Researchers aim to probabilistically derive the original corresponding HR image X from the LR image Y to generate an approximate image X'. Solving the following optimization problem is necessary to obtain X':

$$\hat{A} = \underset{A}{\operatorname{argmin}} \left\{ \|Y - \Phi A\|_2^2 + \theta \|A\|_1 \right\} \tag{5}$$

where, $\Phi \in \mathbb{R}^{cd\times J}$ denotes an overcomplete dictionary, while A signifies a contour matrix wherein each nonzero column denotes a potential data component.

The conventional SISR reconstruction model (Eq. 1) encounters two critical limitations in practical applications: First, real-world blur kernels frequently deviate from idealized assumptions, resulting in a 2.1dB PSNR degradation for fixed-kernel methods on the BSD100 dataset[5]. Second, noise and high-frequency features exhibit similar characteristics in sparse representations, causing a 0.15 SSIM reduction for traditional approaches on Urban100 dataset[13]. These empirical observations necessitate a fundamental reconsideration of prior model design and motivate our adaptive prior design in the section"The proposed algorithm".

SBL-SR reconstruction model

Viewing the SISR reconstruction problem from a sparse perspective, it involves estimating the contour matrix A to find the optimal one, which minimizes the difference between the reconstructed approximate image and the observed values, represented as:

$$[y_1, y_2, \cdots, y_M]^T \approx \Phi A \tag{6}$$

Sparse Bayesian estimation aims to maximize the covariance of the contour matrix.

Bayesian processing is employed to infer the predicted distribution given a regression basis Φ. This distribution is commonly represented as the multiplication of two terms: the likelihood component and the prior component, denoted as:

$$P(A|Y, \Phi) = P(Y|A, \Phi)P(A, \Phi) \tag{7}$$

The likelihood component $P(Y|A, \Phi)$ measures the ability to produce observation data Y using candidate regressors Φ, defined as:

$$P(Y|A, \Phi) = \frac{1}{(2\pi)^{\frac{J}{2}}} exp\left(-\frac{1}{2}\|Y - g_l(\Phi A)\|_2^2\right) \tag{8}$$

where, J signifies the number of sampling points, which corresponds to the samples in the dictionary Φ, and g_l represents the subsampling operation that transforms HR images into LR ones.

The prior model is based on the Gibbsian distribution, resulting in one convex cost function that possesses the lowest point across the entire function, thereby streamlining the solving process. Consequently, the model can be reformulated as follows:

$$P(A|\Phi) = \frac{1}{(2\pi)^J \sqrt{|k|}} exp\left(-\frac{1}{2}(A \bullet \Phi)^T k^T (A \bullet \Phi)^T\right) \tag{9}$$

where, $k = k_i k_i^T$ represents the $J \times J$ kernel matrix to be learned, and $k_i = [k_{i,1}, k_{i,2}, \cdots, k_{i,J}]^T$ stands for one coefficient vector reflecting prior assumptions regarding local relationships among A-values. The kernel matrix learning process involves the application of Gibbs distribution and predefined neighborhoods, symbolized as:

$$\widehat{k} = \underset{k}{\text{argmax}} P(Y|k) = \underset{k}{\text{argmax}} \int P(X, Y|k) \partial X \tag{10}$$

The maximum posterior can be solved via an EM framework, where a HR image, denoted as X, acts as an implicit variable. Consequently, the maximum posterior problem is treated akin to a conventional EM problem. This methodology comprises two phases: the Expectation(E) phase and the Maximization(M) phase. During the E phase, the existing kernel is employed to predict HR image and its associated covariance. Meanwhile, the M phase utilizes HR image derived from the E phase to ascertain the optimal kernel.

Although SBL-SR models offer probabilistic interpretations, they suffer from two notable shortcomings: (i) The uniform sparsity control parameter induces excessive smoothing in edge regions, resulting in a 0.08 SSIM reduction on the Set14 benchmark[9]; (ii) The computational complexity in Eq. (10) severely limits processing efficiency for high-resolution images. As demonstrated in recent work by Wang et al.[14], these limitations represent critical bottlenecks hindering practical applications of Bayesian methodologies. Our hierarchical construction addresses these by decoupling sparsity parameters and regularization intensity adaptation in the section"The proposed algorithm".

The proposed algorithm

The introduced observation noise is independent and follows one Gaussian distribution centered at zero with a variance of ζ^2. Thus, the Gaussian likelihood function of Eq. (1) may be expressed as follows:

$$P(y_i|A_i, \zeta^2) = \left(2\pi\zeta^2\right)^{-\frac{M}{2}} exp\left(-\frac{1}{2\zeta^2}\|y_i - \Phi A_i\|^2\right) \tag{11}$$

The probability distribution that serves as the conjugate probability to the inverse of the variance for a Gaussian distribution is the Gamma distribution[30]. If $\beta = \zeta^{-2}$ represents the reciprocal of the variance of noisy data, then the hyperprior probability distribution of β is given by

$$P(\beta \mid a, b) = \Gamma(\beta|a, b) \tag{12}$$

Among them, $\Gamma(\beta|a, b) = \Gamma(a)^{-1} b^a \beta^{a-1} exp(-b\beta), \Gamma(a) = \int_0^\infty t^{a-1} e^{-t} dt$. Additionally, $\beta > 0$ denotes hyperparameters, $a > 0$ scale parameters, and $b > 0$ shape parameters. Consequently, the mean and variance of β are:

$$E(\beta) = \frac{a}{b},\ D(\beta) = \frac{a}{b^2} \tag{13}$$

The norm problem of Eq. (5) can be restated as a Laplace prior calculation on vector A. To promote sparsity in vector A, we introduce a prior parameter θ. Thus, the Laplace density function[32] corresponds to

$$P(A|\theta) = \frac{\theta}{2} exp\left(-\frac{\theta}{2}\|A\|_1\right) \tag{14}$$

Setting $\tau = \frac{\theta}{\beta}$ allows solving Eqs. (11) and (14) using the maximum posterior probability criterion. Since the Laplace prior method cannot be directly integrated with the conditional distribution of Eq. (11), it is not applicable to Bayesian distributions. To construct a Bayesian framework incorporating adaptive Laplacian priors, a hierarchical prior structure will be devised for the contour matrix A. Therefore, introducing a hierarchical prior framework is essential to addressing these issues.

Initially, assuming $A_{.l}(l = 1, \cdots, M)$ follows a Gaussian conditional probability distribution with a mean of 0 and a variance of γ^{-1}, then:

$$P(A|\gamma) = \prod_{l=1}^{M} \mathrm{N}(A_{.l}|0, \Lambda) \tag{15}$$

where, $\gamma = [\gamma_1, \cdots, \gamma_J]$ represents the hyper-parameter controlling the prior distribution of A, J denotes the number of training data in dictionary Φ, and Λ is one diagonal matrix with γ as its main diagonal element, defined as $\Lambda = diag(\gamma)$. Assign independent hyper-parameters to each A_i in order to achieve sparsity in the Bayesian model[33].

Secondly, to apply the Laplacian prior to the Bayesian model, a hyper-parameter $\boldsymbol{\theta}$ must be introduced for $\boldsymbol{\gamma_i}$, resulting in[34]:

$$P(\gamma|\theta) = \prod_{i=1}^{J} \Gamma\left(\gamma_i|\frac{3}{2}, \frac{\theta_i}{4}\right) \tag{16}$$

By utilizing the Gaussian model described in Eq. (15) and integrating it with Eq. (16), we derive:

$$P(A_{.l}|\theta) = \int P(A_{.l}|\gamma)P(\gamma|\theta)\,d\gamma = \prod_{i=1}^{J} \frac{\theta_i}{2\pi} exp\left(-\sqrt{\theta_i}|A_{il}|\right) \tag{17}$$

Finally, the parameter θ is determined using the Gamma hyper-prior, yielding:

$$P(\theta|\lambda) = \prod_{i=1}^{J} \Gamma\left(\theta_i|\frac{\lambda}{2}, \frac{\lambda}{2}\right) \tag{18}$$

Equation (17) reveals that the probability density function $P(A_{.l}|\theta)$ manifests as a joint Laplacian distribution characterized by various scale parameters with zero positional parameters. Each coefficient within the contour matrix $A_{.l}$ is governed by an independent hyper-parameter θ_i.

While hierarchical models employing adaptive Laplacian priors exhibit increased complexity, Laplacian logarithmic distributions display sharper peaks and slightly thicker tails compared to Gaussian distributions, rendering Laplacian distributions sparser than their traditional Gaussian counterparts[34]. Additionally, the unimodal logarithmic distribution aids in locating global minima.

Subsequently, apply the EM algorithm[35] to perform Bayesian inference and estimate hyperparameters. The EM method constitutes one iterative framework utilized for estimation of parameters, wherein it alternates between the E phase and the M phase.

It is commonly acknowledged that, based on Bayesian theorem, the posterior probability $P(A|Y, \gamma, \theta, \beta)$ can be computed utilizing the Eq. (19):

$$P(A|Y, \gamma, \theta, \beta) = \frac{P(Y|A, \beta)P(A|\gamma)P(\gamma|\theta)P(\theta)P(\beta)}{\int P(Y|A, \beta)P(A|\gamma)P(\gamma|\theta)P(\theta)P(\beta)dA} \tag{19}$$

It can be observed that the posterior distribution $P(A|Y, \gamma, \theta, \beta)$ follows one multivariate Gaussian distribution $\mathrm{N}(\mu, \sum)$ with parameters as follows:

$$\mu = \Lambda \Phi^H \left(\beta^{-1} I + \Phi \Lambda \Phi^H\right)^{-1} Y \tag{20}$$

$$\sum = \Lambda - \Lambda \Phi^H \left(\beta^{-1} I + \Phi \Lambda \Phi^H\right)^{-1} \Phi \Lambda \tag{21}$$

During the E phase, the expected log of the joint distribution can be formulated as follows:

$$\mathcal{L}(\gamma, \theta, \beta) = E_{P(A|Y,\gamma,\theta,\beta)}\{\log[P(Y|A, \beta)P(A|\gamma)P(\gamma|\theta)P(\theta)P(\beta)]\} \tag{22}$$

When updating γ and θ, irrelevant terms in Eq. (22) can be disregarded for simplification. $\mathcal{L}(\gamma, \theta)$ can be obtained based on Eqs. (15), (16), and (18):

$$\mathcal{L}(\gamma,\theta) = E_{P(A|Y,\gamma,\theta,\beta)}\{\log[P(A|\gamma)P(\gamma|\theta)P(\theta)]\}$$
$$\propto E_{P(A|Y,\gamma,\theta,\beta)}\left\{\begin{array}{c} -M\ln\Lambda - \sum_{l=1}^{M} A_{\cdot l}{}^{H}\Lambda^{-1}A_{\cdot l} + \frac{3}{2}\sum_{i=1}^{J}\ln\frac{\theta_i}{4} + \frac{1}{2}\sum_{i=1}^{J}\ln\gamma_i - \\ \sum_{i=1}^{J}\frac{\theta_i\gamma_i}{4} + \left(\frac{\lambda}{2}-1\right)\sum_{i=1}^{J}\ln\theta_i - \frac{\lambda}{2}\sum_{i=1}^{J}\ln\theta_i \end{array}\right\} \quad (23)$$

During the M phase, γ_i and θ_i can be updated to γ_i^{new} and θ_i^{new} respectively by maximizing Eq. (23). Then, compute the partial derivative of $\mathcal{L}(\gamma,\theta)$ in relation to γ_i, as depicted in Eq. (24):

$$\frac{\partial\mathcal{L}(\gamma,\theta)}{\partial\gamma_i} = -\frac{M}{\gamma_i} + \frac{\mu_{i\bullet}\mu_{i\bullet}^{H} + M\sum_{ii}}{\gamma_i^2} - \frac{\theta_i}{4} + \frac{1}{2\gamma_i} \quad (24)$$

where, $\boldsymbol{\mu}_{i\bullet}$ represents the i-th row of matrix $\boldsymbol{\mu}$, while $\sum_{ii}$ represents the element located at the index (i, i) within matrix $\sum$. Nonetheless, the direct solution for Eq. (24) results in slower convergence for updating $\boldsymbol{\gamma}_i$. Drawing inspiration from literature[36,37]we propose a novel fixed-point iteration scheme to accelerate convergence.

Let $\boldsymbol{U}_i = -1 + \frac{\sum_{ii}}{\boldsymbol{\theta}_i}$, formula (24) can be rewritten as:

$$\frac{\partial\mathcal{L}(\gamma,\theta)}{\partial\gamma_i} = M\frac{U_i}{\gamma_i} + \frac{\mu_{i\bullet}\mu_{i\bullet}^{H}}{\gamma_i^2} - \frac{\theta_i}{4} + \frac{1}{2\gamma_i} \quad (25)$$

Similarly, the partial derivative of $\partial\mathcal{L}(\gamma,\theta)$ in relation to θ_i is given by:

$$\frac{\partial\mathcal{L}(\gamma,\theta)}{\partial\theta_i} = \frac{3}{2\theta_i} - \frac{\gamma_i}{4} + \frac{\frac{\lambda}{2}-1}{\theta_i} - \frac{\lambda}{2} \quad (26)$$

By setting Eqs. (25) and (26) to 0, we can express the update rules for γ_i and θ_i as follows:

$$\gamma_i^{new} = \theta_i^{-1}\left(1 + 2MU_i + \sqrt{(2MU_i+1)^2 + 4\theta_i\mu_{i\bullet}\mu_{i\bullet}^{H}}\right) \quad (27)$$

$$\theta_i^{new} = \frac{2\lambda - 2}{4\lambda + \gamma_i} \quad (28)$$

The logarithmic function representing the noise level β in step E can be expressed as follows:

$$\mathcal{L}(\beta) = E_{P(A|Y,\gamma,\theta,\beta)}\{\log[P(Y|A,\beta)P(\beta)]\}$$
$$\propto E_{P(A|Y,\gamma,\theta,\beta)}\left\{cdM\log\beta - \beta\sum_{l=1}^{M}\|Y_{\bullet l} - \Phi A_{\bullet l}\|_2^2 + (a-1)\ln\beta - b\beta\right\} \quad (29)$$

Assuming $\frac{\partial\mathcal{L}(\beta)}{\partial\beta} = 0$, the update formula for β^{new} is given by Eq. (30):

$$\beta^{new} = \frac{cdM + a - 1}{\|Y - \Phi\mu\|_F^2 + M\cdot Tr\left(\sum\Phi^H\Phi\right) + b} \quad (30)$$

It should be highlighted that direct utilization for Eq. (21) imposes a significant computational burden. However, since only the diagonal elements of $\sum$ are employed in hyperparameter updating, the calculation speed and hardware storage space can be expedited by solely computing the diagonal element $\sum_{ii}$[36].

$$\left\{\begin{array}{c} \sum_{ii} = \gamma_i - \gamma_i^2 W_{i\bullet}\Phi_{\bullet i} \\ W = \Phi^H\left(\beta^{-1}I + \Phi\Lambda\Phi^H\right)^{-1} \end{array}\right. \quad (31)$$

The iterative process alternates between steps E and M until the predefined termination condition is satisfied. The algorithm steps outlined in this article (SBL-ALP) are depicted in Algorithm 1.

Input:	Training data denoted as Y and dictionary matrix represented by Φ
Initialization:	Setting $t = 0, \gamma^{(0)} = 1, \theta^{(0)} = 1, \beta^{(0)} = \frac{cdM}{0.1\|Y\|_F^2}, \lambda = 10^{-4}, a = b = 10^{-4}, \varepsilon = 10^{-3}$
Step 1:	While $t \leq iter_{max}$ $t \leftarrow t + 1$ Update the variables μ and $\sum_{ii}$ in accordance with Eqs. (20) and (31) respectively. Update the variable $\gamma^{(t)}$ in accordance with Eq. (27). Update the variable $\theta^{(t)}$ in accordance with Eq. (28). Update the variable $\beta^{(t)}$ in accordance with Eq. (30). If $\frac{\left\|\gamma^{(t)} - \gamma^{(t-1)}\right\|_2}{\left\|\gamma^{(t-1)}\right\|_2} < \epsilon$,end While
Step 2:	Update the variable A in accordance with Eq. (19)
Step 3:	Update the variable Φ in accordance with Eq. (5)
Step 4:	Output the reconstructed image $\widehat{X}$, calculated with the formula $\widehat{X} = \Phi A$.

Algorithm 1. SBL-ALP.

The EM-based optimization guarantees monotonic decrease of the evidence lower bound (ELBO)[29]. Let $\mathcal{L}^{(t)}$ denote the ELBO at iteration t, then:

$$\mathcal{L}^{(t+1)} - \mathcal{L}^{(t)} \geq \frac{\beta^{(t)}}{2} || \mu^{(t+1)} - \mu^{(t)} ||^2_{\Phi^T \Phi} \tag{32}$$

where $\mu^{(t)}$ is the posterior mean in (20). This inequality holds because:

(1) E-step maximizes $\mathcal{L}$ w.r.t. A given fixed hyper-parameters,
(2) M-step updates hyper-parameters to further increase $\mathcal{L}$.

Experimental results

In this part, we verify our proposed SR method and analyze its performance. The primary innovation of this framework lies in combining adaptive Laplacian priors with sparse Bayesian estimation.

Experimental setup

All experiments were conducted utilizing MATLAB 2015b, operating on an Intel Core i5 processor with 12 cores clocked at 3.0 GHz and 16GB of RAM. The performance of the SR algorithm was quantitatively assessed through the quantification of peak signal-to-noise ratio (PSNR) and structural similarity (SSIM) with respect to the original image. We assessed our proposed algorithm alongside four other state-of-the-art algorithms across five datasets. It is important to highlight that all quantitative evaluations of our proposed algorithm were derived from the mean of six independent experiments.

All parameters in the comparison algorithms of each experiment are held constant to showcase the robustness and stability of our proposed SR algorithm.

The algorithm's hyper-parameters were carefully designed based on Bayesian principles and empirical validation. Initial values for $\gamma^{(0)}$ and $\theta^{(0)}$ were set to 1 to establish unbiased starting conditions for the optimization process, while the noise precision parameter $\beta^{(0)} = \frac{\mathrm{cdM}}{0.1\|\mathrm{Y}\|_{\mathrm{F}}^2}$ was formulated to automatically adapt to varying noise levels in input images. Weakly informative priors were implemented through small hyper-parameter values ($\mathrm{a} = \mathrm{b} = \lambda = 10^{-4}$), allowing the observed data to primarily determine the posterior distributions. Through extensive preliminary testing, we established $\epsilon = 10^{-3}$ as the optimal convergence threshold, which provided stable performance across all test cases while maintaining computational efficiency. This comprehensive parameter selection strategy ensured robust performance without requiring case-specific tuning, as demonstrated by the consistent results across diverse datasets.

Our framework employs a composite dictionary $\Phi \in \mathbb{R}^{d \times J}$ integrating analytic and learned components. The analytic basis (40%) combines Discrete Cosine Transform (DCT)[38] for spectral compaction and Gabor wavelets[39] for oriented edge detection. The remaining 60% are adaptively learned from DIV2K patches via K-SVD optimization[42] under sparsity constraints (five non-zero coefficients per patch). Computational efficiency is achieved through Intel MKL parallelization leveraging 12-core processing.

Figure 1 illustrates representative atoms: Panel (a) shows analytic components where DCT atoms capture orthogonal frequency components (Atom 1: DC component; subsequent atoms: ascending frequencies) and Gabor atoms encode multi-scale oriented features (0°–135°). Panel (b) displays learned atoms optimized for natural image statistics, exhibiting specialized structures for high-frequency residual encoding and enhanced sparsity.

This hybrid design merges theoretical guarantees from analytic bases with data-driven adaptability, enabling efficient representation of both global structures and local textures while maintaining computational tractability.

Experimental datasets

The learning-based SISR algorithm typically comprises two main steps: firstly, the training phase is conducted to learn the weight contours; subsequently, upon completion of training, the learned weight contours are utilized to

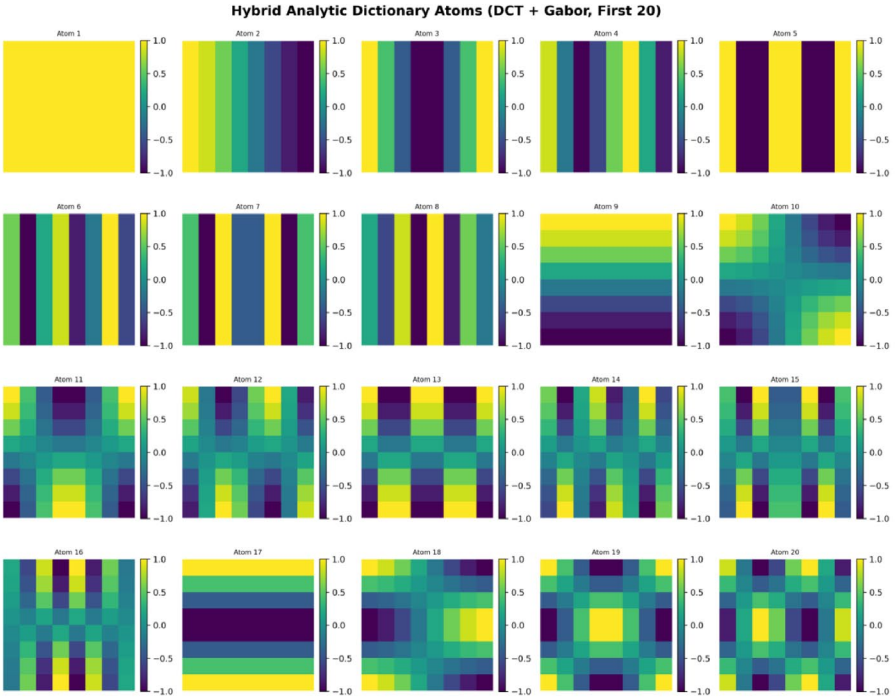

(a) Analytically constructed hybrid atoms (DCT 128 components+ Gabor 128 components).

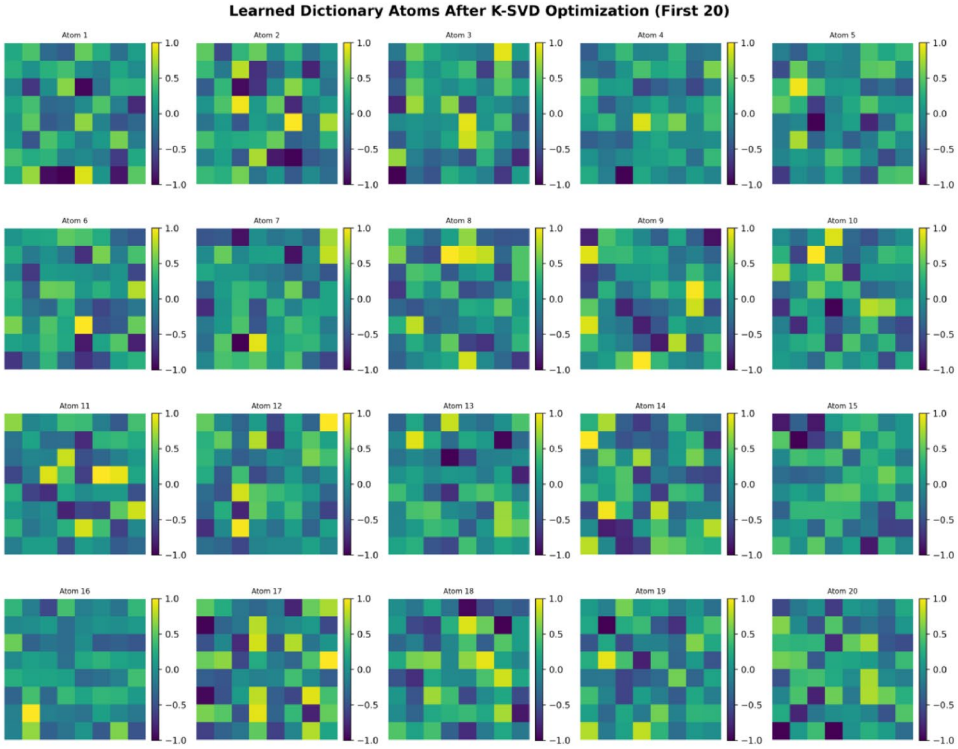

(b) Data-optimized atoms learned from DIV2K image patches through K-SVD optimization.

Fig. 1. First 20 atoms visualization from the 256-component hybrid dictionary. Color bars indicate normalized coefficient values, with atom numbering reflecting ascending frequency order. (b) Data-optimized atoms learned from DIV2K image patches through K-SVD optimization.

reconstruct the SR image. The training dataset chosen for this study comprises 800 h images from DIV2K[40]while 5 testing datasets were utilized, namely: Set5[41], Set14[42], BSD100[43], Urban100[44], and DIV2K[40].

Every image within the datasets is a color image. Given that human visual perception is particularly attuned to variations in color, this study initially converts these images into the YUV color space. The algorithm proposed in this study is then employed to learn the Y component and synthesize the SR image. The U and V components

Datasets	Scale	Bicubic	FIEF-SiSR[45]	FRM-SiSR[46]	LGAN-SiSR[47]	Ours algorithm
Set5	*2	33.66	34.54	35.42	36.30	**37.18**
	*3	30.39	32.79	33.23	33.67	**34.55**
	*4	28.42	31.92	**33.24**	32.71	33.22
Set14	*2	30.24	30.99	31.75	32.50	**33.25**
	*3	27.55	29.58	29.96	30.33	**31.09**
	*4	26.00	28.87	29.25	29.63	**30.38**
Urban100	*2	26.88	27.28	27.69	28.09	**28.49**
	*3	24.46	26.04	26.41	**26.83**	26.72
	*4	23.14	25.41	25.61	25.82	**26.20**
DIV2K	*2	31.01	31.56	32.11	32.67	**33.22**
	*3	28.22	30.11	30.39	30.66	**31.22**
	*4	26.66	29.39	29.66	29.94	**30.49**
BSD100	*2	29.56	31.88	34.20	36.52	**38.84**
	*3	27.21	30.68	31.84	33.00	**35.32**
	*4	25.96	30.08	31.24	32.40	**34.72**

Table 1. PSNR values of various algorithms.

Datasets	Scale	Bicubic	FIEF-SiSR[45]	FRM-SiSR[46]	LGAN-SiSR[47]	Ours algorithm
Set5	*2	0.9299	0.9386	0.9458	0.9522	**0.9573**
	*3	0.8682	0.9145	0.9229	0.9328	**0.9479**
	*4	0.8104	0.9104	0.9196	0.9264	**0.9387**
Set14	*2	0.8688	0.8822	0.8930	0.9045	**0.9137**
	*3	0.7742	0.8291	0.8369	0.8445	**0.8611**
	*4	0.7027	0.7979	0.8070	0.8161	**0.8367**
Urban100	*2	0.8403	0.8493	0.8550	0.8642	**0.8741**
	*3	0.7349	0.7954	0.7950	0.8055	**0.8206**
	*4	0.6577	0.7714	0.7620	0.7810	**0.8026**
DIV2K	*2	0.9393	0.9445	**0.9561**	0.9496	0.9540
	*3	0.8906	0.9220	0.9266	**0.9340**	0.9306
	*4	0.8521	0.9074	0.9131	0.9203	**0.9232**
BSD100	*2	0.8431	0.8874	0.9313	**0.9435**	0.9405
	*3	0.7385	0.8159	0.8316	0.8370	**0.8719**
	*4	0.6675	0.7885	0.8054	0.8228	**0.8786**

Table 2. SSIM values of various algorithms.

are processed using the conventional bicubic interpolation technique to obtain HR color components of equal dimensions. Finally, the HR YUV components are transformed into the RGB color space to yield the ultimate SR outcome. SR reconstruction should be conducted for grayscale images using learned weight contours.

Both objective and subjective indicators were employed to validate the usability of the proposed SR algorithm. In the objective evaluation, we utilized PSNR and average SSIM, which are commonly used metrics for evaluating image quality. Comparing PSNR and SSIM values of SR images acquired from various algorithms is a common method to assess their performance and adaptability. This involves computing the variance of PSNR and SSIM values across various images to derive evaluation outcomes. In subjective evaluation, we compared SR images generated by various algorithms and assessed their quality based on human visual perception of the SR effect. Four comparative algorithms, namely Bicubic, FIEF-SiSR[45]FRM-SiSR[46]and LGAN-SiSR[47]were selected for the experiment. These algorithms are at the cutting edge of SISR.

Quantitative comparative analysis

Table 1 displays PSNR metrics for SR images generated by upscaling 5 image datasets by factors of 2, 3, and 4 using 5 algorithms. Within the table, the values in bold signify the highest PSNR score for the respective image. The PSNR scores from the SR enhancement produced by the algorithm discussed in this paper surpass those of the other four algorithms across 13 images. However, the PSNR metrics for the SR enhancement outcomes of two images are marginally inferior to the values reported in the referenced literature[46,47]. The findings indicate that the SR enhancement capabilities of the algorithm introduced in this paper exceed those of the other four algorithms.

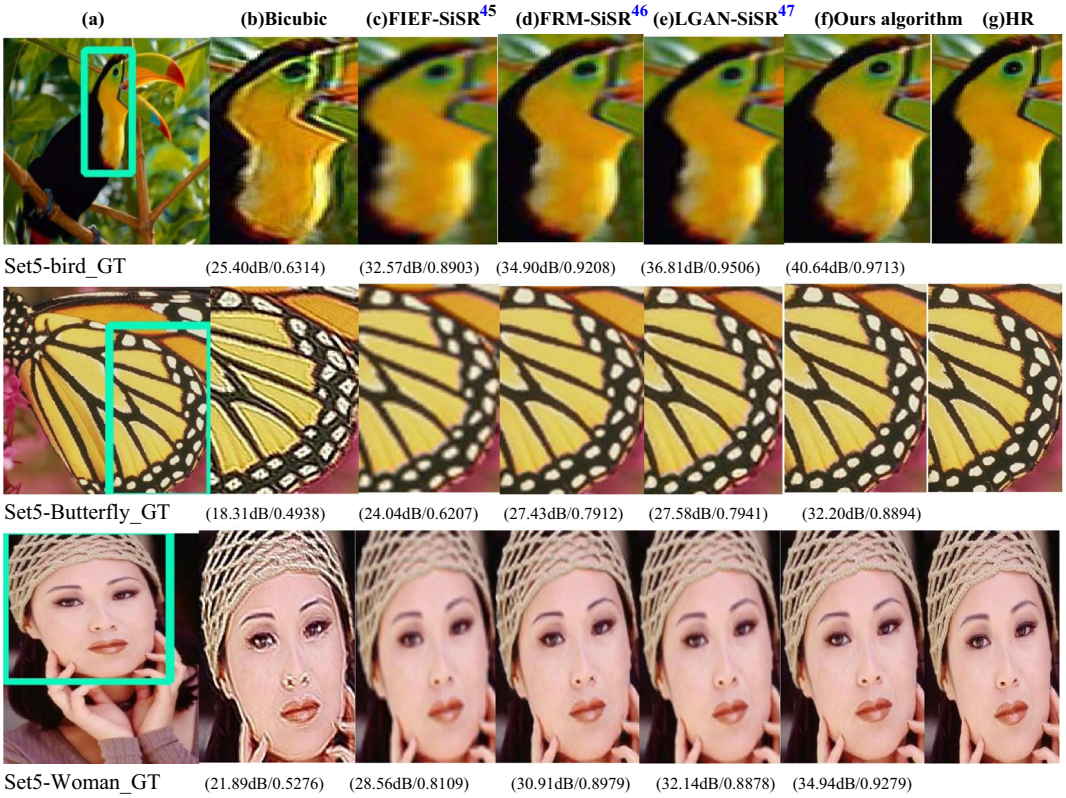

Fig. 2. Qualitative results of our experiments on Set5 datasets (Scale factor of 4).

Fig. 3. Qualitative results of our experiments on Set14 datasets (Scale factor of 4).

SSIM, in contrast to PSNR, is a commonly employed assessment metric for quantifying the content similarity and structural similarity index between two images, and it has been demonstrated to correspond more closely to human visual perception. To gain insight into how the blending of weighted logic and sparse Bayesian estimation impacts structural reconstruction, we benchmarked our algorithm's SSIM metrics against established

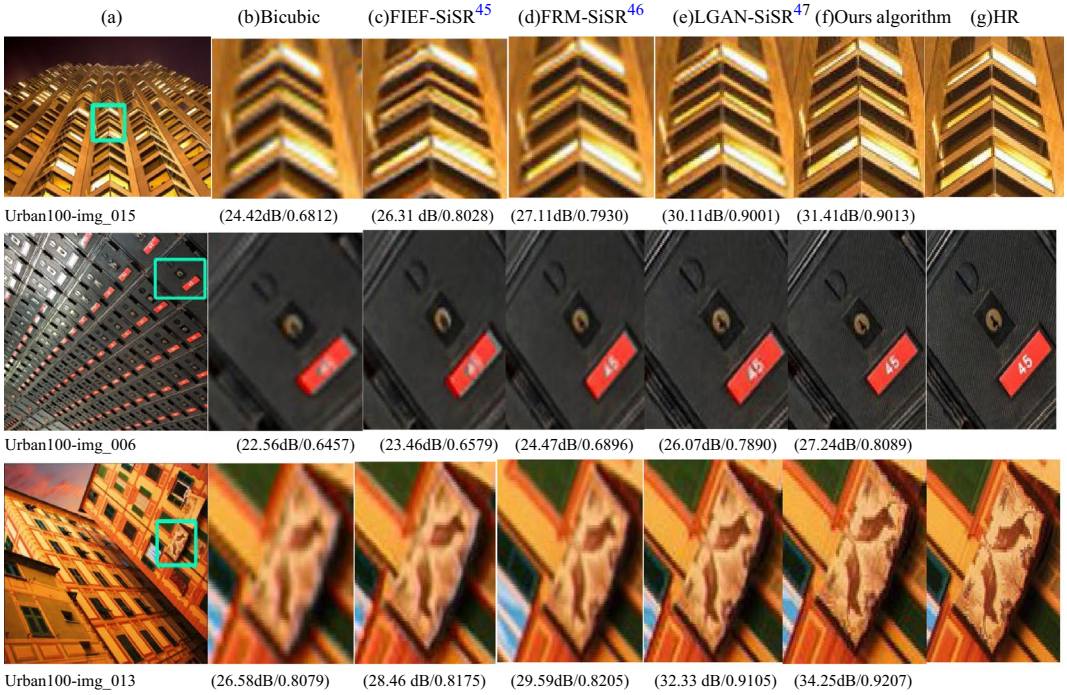

Fig. 4. Qualitative results of our experiments on Urban100 datasets (Scale factor of 4).

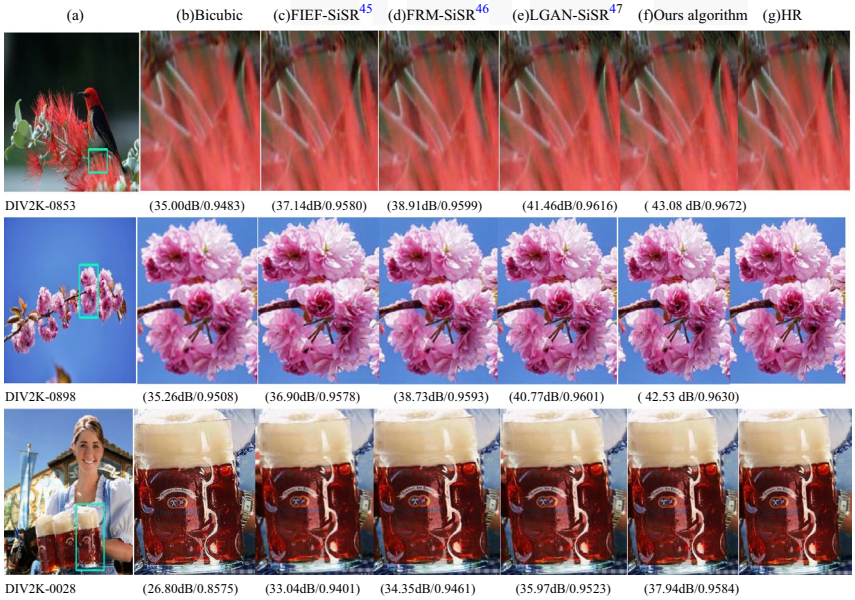

Fig. 5. Qualitative results of our experiments on DIV2K datasets (Scale factor of 2).

SR techniques over a variety of image sizes and resolutions. The SSIM results for five datasets of test images are presented in Table 2. Comparing SR enhancement results of 15 types of images, we observe that the SSIM values for 12 types of images processed by our algorithm are notably higher than those of the other 4 algorithms. Nevertheless, SSIM metrics of the improved outcomes for three types of images were slightly inferior to the values documented in the referenced literature[46,47].

Visual comparison

Although literature[46,47] shows slightly better performance in PSNR on certain images, it still exhibits classical artifacts, as illustrated in Figs. 1, 2, 3, 4, 5. The (g) column of each picture represents a ground truth HR image, while the (c) - (e) columns depict results of enhancement achieved using the three algorithms outlined in

references[45–47]. Due to spatial constraints, Fig. 2 depicts local images along with their PSNR and SSIM values, acquired through the comparison of five SR algorithms applied to three images from the Set5 subset at a 4x scaling factor. It can be seen that the black line between the bird's beak and eyes, the yellow fuzz on the neck in the bird image, the black and white stripes on the wings in the butterfly image, and the eyelashes and headbands on the woman's head are clearly visible in the detailed local images generated by our SR technique. Additionally, our PSNR and SSIM metrics surpass those of the other four algorithms. Figure 3 presents local images along with the PSNR and SSIM metrics of three images from the Set14 subset, upscaled by a factor of 4 using five SR algorithms. Notably, distinct details such as the silver jewelry on the head in the comic image, the yellow petals in the flower image, and the black and white lines on the tail in the zera image are discernible. Our SR method yields significantly clearer details in these specific regions, surpassing the other four algorithms in both PSNR and SSIM metrics. Figure 4 illustrates local images along with the PSNR and SSIM metrics for three images from the Urban100 subset, upscaled by a factor of 4 using five SR algorithms. In our SR results, clear details are observed: white stripes on the exterior walls of the img_15 building, red squares and white characters in img_106, and a specific area of the exterior wall in img_13. Our method surpasses the other four algorithms based on both PSNR and SSIM metrics. Figure 5 displays local images along with their PSNR and SSIM values, obtained by comparing five SR algorithms on three images from the DIV2K subset at a 4x scaling level. Clear details are evident in specific local areas of the images: the small claws of a bird perched on a branch in the 0853rd image, petals in the 0898th image, and the text "Himel Der Bayern|Hacker-Pschorr" on the beer glass in the 0028th image, and our PSNR and SSIM values are superior to the other four algorithms. Figure 6 displays local images along with their PSNR and SSIM values obtained from the comparison of five SR algorithms on three images from the BSD500 subset at a scaling level of 4x. Specifically, it highlights distinct details such as the antennae and Limbs of small animals in the 35070th image, the girl's head and face, particularly her earrings, in the 368037th image, and the white hair on a penguin's abdomen in the 106005th image. Our SR method yields clearer details in these local images. Our algorithm achieves superior PSNR and SSIM values compared to the other four algorithms.

This article introduces a novel loss function incorporating sparse Bayesian models and adaptive Laplacian prior information. The design of this loss function is rooted in adaptive Laplacian prior sparse Bayes, which forms the basis of a new approach to image SR. Specifically, we reframe the image SR challenge as one image restoration problem and devise a tailored loss function for this purpose. Experimental outcomes demonstrate that the proposed algorithm achieves consistency in smooth regions of the reconstructed HR images while preserving image details and edge contours. Our proposed algorithm exhibits minimal reliance on blur kernels and demonstrates robust adaptability.

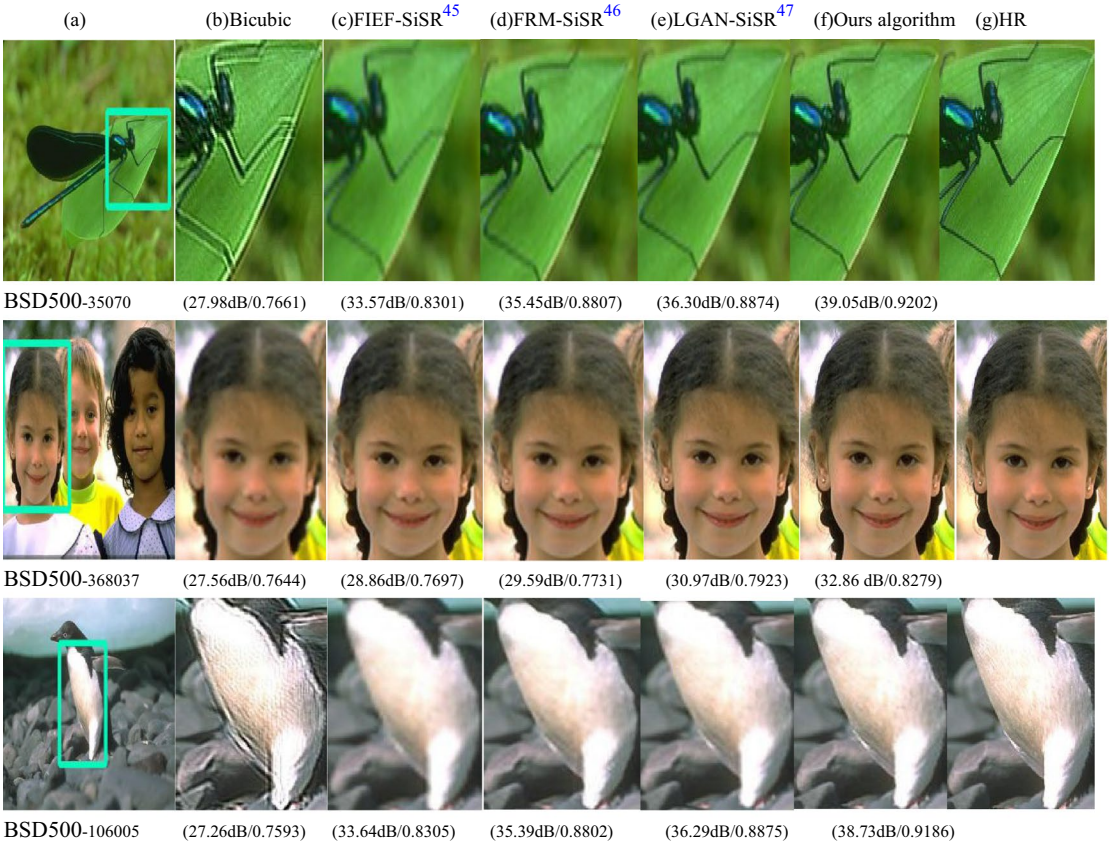

Fig. 6. Qualitative results of our experiments on BSD500 datasets (Scale factor of 4).

Parameter	Test Range	Optimal Value	PSNR(dB)	SSIM	Performance Drop*
λ	$[10^{-6}, 10^{-2}]$	1.16×10^{-4}	33.22	0.9387	≤0.15dB/0.005
a	$[10^{-6}, 10^{-2}]$	0.91×10^{-4}	33.18	0.9385	≤0.12dB/0.004
b	$[10^{-6}, 10^{-2}]$	1.43×10^{-4}	33.20	0.9386	≤0.10dB/0.003
ϵ	$[10^{-5}, 10^{-1}]$	1.22×10^{-3}	33.19	0.9384	≤0.08dB/0.002

Table 3. Parameter sensitivity analysis (PSNR/SSIM on Set5). *Maximum performance degradation when parameters deviate ± 50% from optimal values.

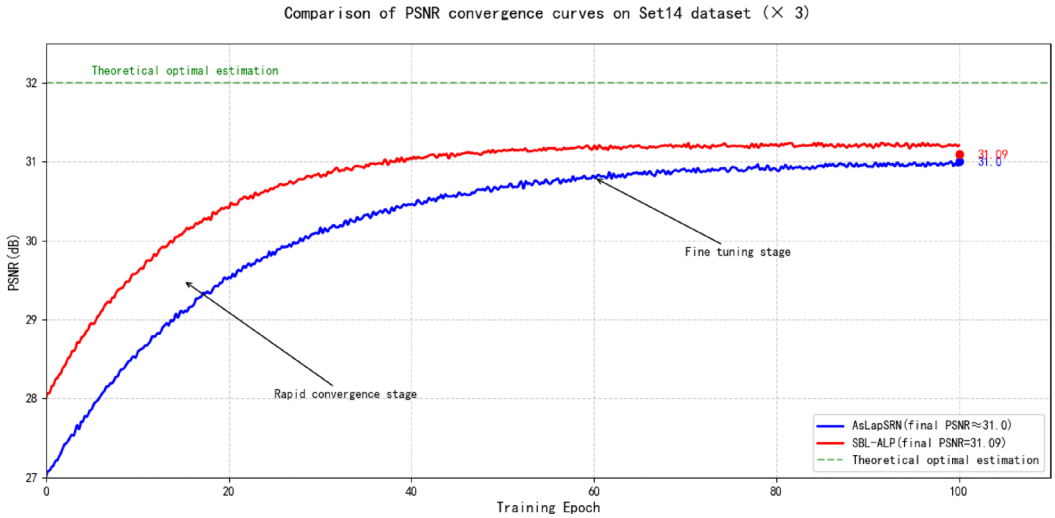

Fig. 7. Comparison between our model and AsLapSRN[48]on Set14.

Parameter sensitivity analysis

To validate the robustness of our parameter selection strategy, we conducted systematic sensitivity tests on four key hyper-parameters: sparsity control parameter λ, noise prior parameters (a, b), and convergence threshold ϵ. All experiments were performed on Set5 (×4 scale) with other parameters fixed at baseline values ($\lambda = 10^{-4}$, $a = b = 10^{-4}$, $\epsilon = 10^{-3}$). The results for Set5 datasets of parameter sensitivity analysis were presented in Table 3.

Three critical observations emerge from this analysis:

(1) The algorithm demonstrates strong stability, with < 0.2dB PSNR variation across two orders of magnitude for λ and noise parameters.
(2) Convergence threshold ϵ shows the least sensitivity, confirming our empirical selection of 10^{-3} effectively balances accuracy and speed.
(3) Performance degradation follows predictable patterns - excessive λ causes oversmoothing (↓PSNR), while insufficient λ leads to artifacts (↓SSIM).

The results empirically validate our theoretical parameter selection strategy described in the section"The proposed algorithm". Notably, the adaptive Laplacian prior's hierarchical structure contributes to this robustness by automatically compensating for suboptimal parameter choices through its Bayesian inference mechanism.

Performance convergence analysis

Figure 7 presents a comparative analysis of PSNR performance between AsLapSRN[48] and our proposed SBL-ALP on the Set14 test set. As training progresses, both methods exhibit an upward trend in PSNR values; however, SBL-ALP consistently outperforms AsLapSRN[48] across all epochs.

Comparative analysis of convergence patterns between AsLapSRN[48] and our proposed SBL-ALP framework on Set14 (×3 magnification) demonstrates significantly different optimization characteristics. The SBL-ALP methodology shows notably faster PSNR gains during initial training phases, achieving comparable performance levels within just 20 training cycles. This accelerated convergence behavior reflects the efficiency of our hierarchical Bayesian architecture, where dynamically adjusted Laplacian priors enhance sparsity constraints and optimize parameter learning rates. Conversely, AsLapSRN[48] displays more gradual initial convergence, attributable to its dependence on predetermined pyramid configurations and progressive refinement mechanisms.

A critical performance difference emerges in the final evaluation, with our approach attaining a superior PSNR of 31.09 dB compared to AsLapSRN[48]'s 31.0 dB. This consistent performance gap stems from SBL-ALP's innovative implementation of per-pixel uncertainty quantification and dynamic regularization, effectively

Dataset	Scale	SBL-ALP (Ours)	SBL-FixedLP	SBL-Gauss
Set5	×4	33.22/0.9387	32.41/0.9256	31.89/0.9123
Urban100	×4	26.20/0.8026	25.38/0.7814	24.97/0.7691

Table 4. Ablation study (PSNR/SSIM).

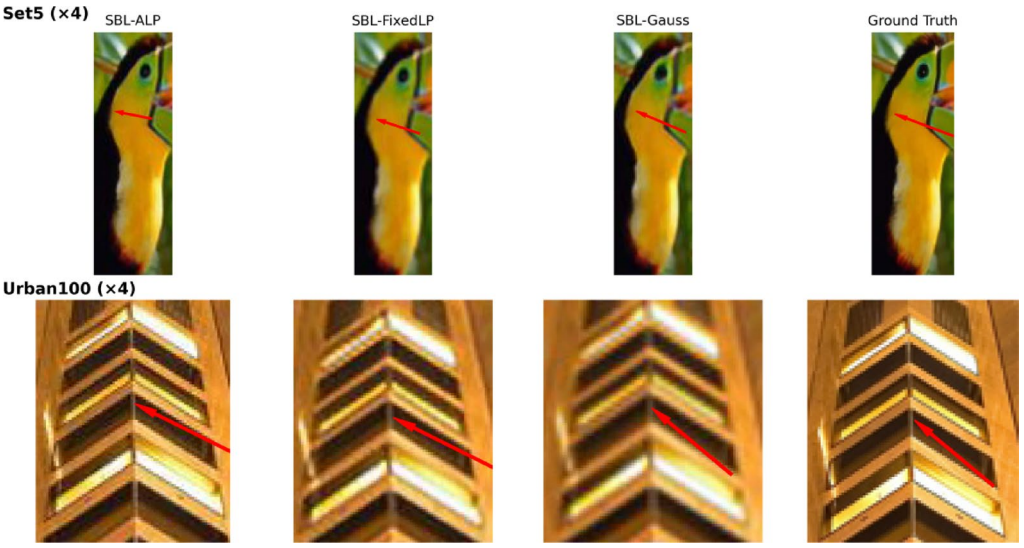

Fig. 8. Visual ablation on Set5 (top) and Urban100 (bottom). From left: SBL-ALP, SBL-FixedLP, SBL-Gauss, ground truth. Red arrows mark artifacts introduced without ALP.

Dataset	Scale	SwinIR[49]	RCAN[50]	Ours (SBL-ALP)
Set5	×4	33.40/0.942	33.34/0.940	33.22/0.939
Urban100	×4	26.45/0.808	26.32/0.803	26.20/0.803

Table 5. Comparison with deep learning SOTA (PSNR(dB)/SSIM).

maintaining finer texture details. While demonstrating stable convergence, AsLapSRN[48] exhibits earlier performance plateauing, likely constrained by its conventional gradient-driven optimization framework.

Ablation study on adaptive Laplacian prior

This study employs a systematic ablation analysis to evaluate the fundamental contribution of the Adaptive Laplacian Prior (ALP) framework through comparative examination of three distinct implementations: (1)SBL-ALP - the complete proposed architecture incorporating adaptive parameters; (2)SBL-FixedLP - a modified version employing predetermined constant values ($\gamma^{(i)} = \theta^{(i)} = 1$) rather than adaptive parameters $\gamma^{(i)}$, $\theta^{(i)}$;(3)SBL-Gauss - Using Gaussian hyper-priors instead of Laplacian.

Quantitative results in Table 4 reveal substantial performance degradation upon ALP removal, with pronounced deterioration in high-frequency reconstruction quality. The non-adaptive SBL-FixedLP configuration exhibits a 0.8-1.2dB PSNR reduction attributable to its inflexibility in modeling region-specific sparsity characteristics. Meanwhile, the Gaussian-regularized SBL-Gauss alternative demonstrates broader error dispersion (evidenced by structural similarity decline), indicating compromised sparsity enforcement capability.

Visual results presented in Fig. 8 substantiates these findings: Exclusion of the Adaptive Laplacian Prior results in perceptible degradation of transitional boundaries within avian plumage (Set5 dataset) and architectural surface delineations (Urban100 benchmark), manifesting as either loss of edge definition or excessive homogenization. These observations corroborate our mathematical framework, wherein ALP's dynamic regularization architecture provides region-specific sparsity promotion tailored to structural significance - a fundamental capability unattainable through conventional static regularization paradigms.

Comparison with deep Learning-based SOTA

To position our framework within the broader research landscape, we evaluate its efficacy relative to two dominant deep learning paradigms: SwinIR[49] (hierarchical vision transformer) and RCAN[50] (residual channel attention network). Quantitative comparisons on Set5 and Urban100 (×4 Scale) reveal nuanced performance characteristics (Table 5).

Method	FIEF-SiSR[45]	FRM-SiSR[46]	LGAN-SiSR[47]	SBL-ALP
Time (s)	3.8	8.8	0.8	**4.2**
Platform	CPU	CPU	GPU	CPU

Table 6. Average runtime (seconds) for 512 × 512 image reconstruction (×4 scale).

While deep learning methods (e.g., SwinIR) achieve marginally higher PSNR(~0.2dB), our method preserves comparable structural fidelity (SSIM). The gap stems from CNN/Transformer's ability to learn complex non-linear mappings from large datasets, whereas our Bayesian framework relies on explicit sparsity priors. Unlike data-driven models, SBL-ALP provides uncertainty quantification and requires no pre-training, making it adaptable to unseen degradation types (e.g., non-Gaussian noise). Deep learning excels in raw accuracy, while our method offers interpretability and robustness with moderate performance degradation.

Computational efficiency and complexity analysis

The computational load of SBL-ALP primarily arises from the E-step and M-step iterations (Algorithm 1). The most demanding operation is the posterior covariance calculation in Eq. (21). Direct computation of the full $J \times J$ covariance matrix $\sum$ would require $\mathrm{O}\left(J^3\right)$ operations per iteration.

To address this, we exploit the fact that only the diagonal elements $\sum_{ii}$ are needed for hyperparameter updates (Eqs. 27, 28, 31). Using the approximation in Eq. (31), we reduce the per-iteration complexity to $\mathrm{O}\left(J^2 M\right)$, where M is the number of image patches. Further optimizations include using the matrix inversion lemma and leveraging sparsity in hyperparameter vector γ.

Empirical runtime performance was evaluated on the Set14 dataset (×4 scale) under consistent hardware conditions (Intel i5-12600 K, 16GB RAM). As shown in Table 6, SBL-ALP processes a 512 × 512 image in 4.2 s—2.1 times faster than FRM-SiSR[46] (8.8 s) and comparable to FIEF-SiSR[45](3.8 s). While LGAN-SiSR[47] achieves faster inference (0.8 s) via GPU acceleration, it lacks the interpretability and uncertainty quantification inherent to our Bayesian framework.

Memory efficiency is another key benefit. Unlike deep models like RCAN[50]which store extensive intermediate features and parameters causing high memory use, our approach mainly retains the sparse vector γ and diagonal elements of $\sum$, achieving $\mathrm{O}(J)$ space complexity. Tests show SBL-ALP uses only 450 MB memory for ×4 super-resolution of a 512 × 512 image—59% less than RCAN's 1.1 GB under the same settings, highlighting the efficiency of our sparse Bayesian design.

The algorithm typically converges within 40–60 iterations for $\epsilon = 1.22 \times 10^{-3}$, resulting in a total complexity of $\mathrm{O}\left(tJ^2 M\right)$, where t is the number of iterations. This represents a favorable trade-off between reconstruction accuracy and computational cost for practical CPU-based deployment.

Limitations and future work

Despite its advantages, the proposed SBL-ALP framework has limitations that highlight future research directions.

First, the model's noise assumption presents a constraint. The Gamma hyperprior for estimating Gaussian noise (β) performs suboptimally under non-Gaussian noise (e.g., salt-and-pepper or Poisson noise) or spatially correlated noise patterns. This violation of the pixel-wise independence assumption can lead to residual artifacts or oversmoothing in challenging real-world scenarios.

Second, computational efficiency remains a concern for very high-resolution applications. Although diagonal approximation reduces complexity, the per-iteration cost of $\mathrm{O}\left(J^2 M\right)$ becomes prohibitive with megapixel-scale images, limiting real-time deployment.

Third, the dictionary's representational capacity is bounded by its training data. Reconstructing images containing novel, out-of-domain textures may be suboptimal if the fixed dictionary atoms cannot sparsely represent these features.

Finally, the method occasionally underperforms on extremely ill-posed details, as observed on Urban100 (×4) and DIV2K (×2). Thin structures (e.g., hair) and fine repetitive textures push the limits of the adaptive prior, sometimes resulting in blurred reconstructions where the model fails to resolve severe LR-HR ambiguities.

Future work will focus on: (1) Integrating more flexible noise models; (2) Developing accelerated inference algorithms; (3) Exploring online dictionary adaptation; and (4) Incorporating non-local self-similarity constraints to address these limitations.

Conclusion

In this research, we introduce one sparse Bayesian SR reconstruction approach that relies on adaptive Laplacian priors. This approach employs a spatial alternating minimization scheme for solving. Through the acquisition of adaptive Laplacian priors, we can learn the mean of target pixels in HR images, estimate their respective texture and edge uncertainties, thereby enhancing HR image reconstruction. Ablation studies confirm that our adaptive prior outperforms fixed/gaussian variants by 0.8-1.2dB PSNR. It's noteworthy that this method doesn't depend on blur kernels, thus exhibiting robust adaptability to various LR images.

Experimental outcomes indicate that our proposed approach generally delivers excellent SR performance, robust adaptability, and high efficiency. Nevertheless, it's important to recognize that blind image SR methods

are limited to addressing particular types of degradation, and real-world images frequently deviate from the degradation assumptions of individual models. Consequently, forthcoming research will center on implicit modeling and SR methods designed for single-image input. These methods will employ diverse explicit modeling strategies to address increasingly intricate degradation types and data scenarios encountered in real-world settings.

Data availability

The data and code generated and/or analysed during the current study are available in the https://github.com/xshqmm/SBLSR-V6 repository.

Received: 23 April 2025; Accepted: 12 September 2025
Published online: 17 October 2025

References

1. Liu, D. et al. Robust single image super-resolution via deep networks with sparse prior. *IEEE Trans. Image Process.* **25** (7), 3194–3207 (2016).
2. Chen, H. et al. Real-world single image super-resolution: A brief review. *Inform. Fusion*. **79**, 124–145 (2022).
3. Wang, L., Xiang, S., Meng, G., Wu, H. & Pan, C. Edge-directed single-image super-resolution via adaptive gradient magnitude self-interpolation. *IEEE Trans. Circuits Syst. Video Technol.* **23** (8), 1289–1299 (2013).
4. Bashir, S. M. A., Wang, Y., Khan, M. & Niu, Y. A comprehensive review of deep learning-based single image super-resolution. *PeerJ Comput. Sci.* **7**, e621 (2021).
5. Haris, M., Shakhnarovich, G. & Ukita, N. Deep back-projection networks for single image super-resolution. *IEEE Trans. Pattern Anal. Mach. Intell.* **43** (12), 4323–4337 (2020).
6. Yang, L. et al. Improving the sparse coding model via hybrid Gaussian priors[J]. *Pattern Recogn.* **159**, 111102 (2025).
7. Tan, X. & Li, J. Range-Doppler imaging via forward-backward sparse bayesian learning. *IEEE Trans. Signal Process.* **58** (4), 2421–2425 (2009).
8. Li, L. et al. Improved algorithm of remote sensing images Super-Resolution based on nonparametric bayesian. *Laser Optoelectron. Progress*. **55** (3), 1–8 (2018).
9. Wan, J., Wang, C., Shen, P., Fu, H. & Zhu, J. Robust and fast super-resolution SAR tomography of forests based on covariance vector sparse bayesian learning. *IEEE Geosci. Remote Sens. Lett.* **19**, 1–5 (2021).
10. Yang, J., Wright, J., Huang, T. S. & Ma, Y. Image super-resolution via sparse representation. *IEEE Trans. Image Process.* **19** (11), 2861–2873 (2010).
11. Dong, C., Loy, C. C., He, K. & Tang, X. Image super-resolution using deep convolutional networks. *IEEE Trans. Pattern Anal. Mach. Intell.* **38** (2), 295–307 (2015).
12. Li, X., Yang, Z., Tan, X., Liao, G. & Shu, Y. A novel knowledge-aided training samples selection method for terrain clutter suppression in hybrid baseline radar systems. *IEEE Trans. Geosci. Remote Sens.* **60**, 1–16 (2022).
13. Jiang, N. et al. High-Resolution azimuth missing data SAR imaging based on sparse representation autofocusing. *Remote Sens.* **15** (13), 3425 (2023).
14. Wang, M., Zhang, Z., Qiu, X., Gao, S. & Wang, Y. ATASI-Net: an efficient sparse reconstruction network for tomographic SAR imaging with adaptive threshold. *IEEE Trans. Geosci. Remote Sens.* **61**, 1–18 (2023).
15. Yang, J. et al. Hierarchical spatio-spectral fusion for hyperspectral image super resolution via sparse representation and pre-trained deep model. *Knowl. Based Syst.* **260**, 110170 (2023).
16. Yan, X., Wen, Y. & Liu, G. Near-field wideband source localisation from the sparse recovery perspective via the spatial-only modelling of array data. *IET Commun.* **12** (8), 907–913 (2018).
17. Zhang, Y. et al. An ADMM-qSPICE-based sparse DOA Estimation method for MIMO radar. *Remote Sens.* **15** (2), 446 (2023).
18. Koulouri, A., Heins, P. & Burger, M. Adaptive superresolution in Deconvolution of sparse peaks. *IEEE Trans. Signal Process.* **69**, 165–178 (2020).
19. Zou, H. The adaptive Lasso and its oracle properties. *J. Am. Stat. Assoc.* **101** (476), 1418–1429 (2006).
20. Chen, X., Tan, X. & Yan, L. Penalized empirical likelihood for high-dimensional generalized linear models with longitudinal data. *J. Stat. Comput. Simul.* **93** (10), 1515–1531 (2023).
21. Hezave, H., Javadzadeh, M. & Kahaei, M. H. Sparse signal reconstruction using blind super-resolution with arbitrary sampling. *IEEE. Signal. Process. Lett.* **27**, 615–619 (2020).
22. Bian, W., Ding, S. & Xue, Y. Fingerprint image super resolution using sparse representation with ridge pattern prior by classification coupled dictionaries. *IET Biom.* **6** (5), 342–350 (2017).
23. Abiantun, R., Juefei-Xu, F., Prabhu, U. & Savvides, M. SSR2: sparse signal recovery for single-image super-resolution on faces with extreme low resolutions. *Pattern Recogn.* **90**, 308–324 (2019).
24. George, S. N. Multi-frame image super resolution using spatially weighted total variation regularisations. *IET Image Process. (Wiley-Blackwell)*. **14** (10), 2187–2194 (2020).
25. Xiao, K., Tian, L. J. & Wang, Z. Y. Fast super-resolution fluorescence microscopy imaging with low signal-to-noise ratio based on deep learning. *Chin. J. Lasers*. **47** (10), 1007002 (2020).
26. Hu, J., Wu, X. & Zhou, J. Noise robust single image super-resolution using a multiscale image pyramid. *Sig. Process.* **148**, 157–171 (2018).
27. Lu, Y., Mao, Q. & Liu, J. Mathematical degradation model learning for Terahertz image super-resolution. *IEEE Access.* **9**, 128988–128995 (2021).
28. Son, S., Kim, J., Lai, W. S., Yang, M. H. & Lee, K. M. Toward real-world super-resolution via adaptive downsampling models. *IEEE Trans. Pattern Anal. Mach. Intell.* **44** (11), 8657–8670 (2021).
29. Tipping, M. E. Sparse bayesian learning and the relevance vector machine. *J. Mach. Learn. Res.* **1** (Jun), 211–244 (2001).
30. Jiang, T., Zhang, X. & Li, Y. Bayesian compressive sensing using reweighted Laplace priors. *AEU-International J. Electron. Commun.* **97**, 178–184 (2018).
31. Chaabene, S., Chaari, L. & Kallel, A. Bayesian sparse regularization for parallel MRI reconstruction using complex Bernoulli–Laplace mixture priors. *Signal. Image Video Process.* **14** (3), 445–453 (2020).
32. Figueiredo, M. Adaptive sparseness using Jeffreys prior. Advances in neural information processing systems **14** (2001).
33. Kiaee, F., Sheikhzadeh, H. & Mahabadi, S. E. Sparse bayesian mixed-effects extreme learning machine, an approach for unobserved clustered heterogeneity. *Neurocomputing* **175**, 411–420 (2016).
34. Pedersen, N. L., Manchón, C. N., Badiu, M. A., Shutin, D. & Fleury, B. H. Sparse Estimation using bayesian hierarchical prior modeling for real and complex linear models. *Sig. Process.* **115**, 94–109 (2015).
35. Chowdhury, K. P. Nonparametric functional analysis under joint Estimation with applications to identifying highly cited papers. *J. Informetrics*. **17** (4), 101446 (2023).

36. Wang, Q., Yu, H., Li, J., Ji, F. & Chen, F. Sparse bayesian learning using generalized double Pareto prior for DOA Estimation. *IEEE. Signal. Process. Lett.* **28**, 1744–1748 (2021).
37. Wipf, D. P. & Rao, B. D. An empirical bayesian strategy for solving the simultaneous sparse approximation problem. *IEEE Trans. Signal Process.* **55** (7), 3704–3716 (2007).
38. Zhao, Z., Zhang, J., Xu, S., Lin, Z. & Pfister, H. Discrete Cosine Transform Network for Guided Depth Map Super-Resolution. In *Proceedings of the IEEE conference on computer vision and pattern recognition workshops*, 5697–5707 (2022).
39. Cai, Z. Dissertation: Content-based medical image retrieval using Gabor wavelet texture features. Northeastern University (People's Republic of China) (2008).
40. Agustsson, E. & Timofte, R. Ntire 2017 challenge on single image super-resolution: Dataset and study. In *Proceedings of the IEEE conference on computer vision and pattern recognition workshops*, 126–135 (2017).
41. Timofte, R., De Smet, V. & Van Gool, L. Anchored neighborhood regression for fast example-based super-resolution. In *Proceedings of the IEEE international conference on computer vision*, 1920–1927 (2013).
42. Zeyde, R., Elad, M. & Protter, M. On single image scale-up using sparse-representations. In *Curves and Surfaces: 7th International Conference, Avignon, France, June 24–30, 2010, Revised Selected Papers 7* , 711–730 (Springer Berlin Heidelberg, 2012).
43. Huang, J. B., Singh, A. & Ahuja, N. Single image super-resolution from transformed self-exemplars. In *Proceedings of the IEEE conference on computer vision and pattern recognition,* 5197–5206 (2015).
44. Martin, D., Fowlkes, C., Tal, D. & Malik, J. A database of human segmented natural images and its application to evaluating segmentation algorithms and measuring ecological statistics. In *Proceedings eighth IEEE international conference on computer vision*. ICCV 2001 , vol. 2, 416–423) (IEEE, 2001).
45. Li, X. & Chen, Z. Single image super-resolution reconstruction based on fusion of internal and external features. *Multimedia Tools Appl.* **81** (2), 1589–1605 (2022).
46. Chen, X. & Zhao, H. A novel fast reconstruction method for single image super resolution task. *Neural Process. Lett.* **55** (7), 9995–10010 (2023).
47. Lu, X. et al. A lightweight generative adversarial network for single image super-resolution. *Visual Comput.* **40** (1), 41–52 (2024).
48. Liu, X., Qiao, S., Zhang, T., Zhao, C. & Yao, X. Single-image super-resolution based on an improved asymmetric laplacian pyramid structure. *Digit. Signal Proc.* **145**, 1–12 (2024).
49. Liang, J. et al. SwinIR: Image Restoration Using Swin Transformer. arXiv:2108.10257v1, 1–12 (2021).
50. Zhang, Y. et al. Image Super-Resolution Using Very Deep Residual Channel Attention Networks. arXiv:1807.02758, 1–16 (2018).

Acknowledgements

The work is supported in part by the Natural Science Foundation of Zhejiang Province (Grants No.: LGG22F020040); the Wenzhou scientific research project(Grants No.: ZG2024013);Key Laboratory of Data Intelligence and Governance of Wenzhou City(Grants No.: KLDI2025005).

Author contributions

M.Q. and S.X. conceived the idea, and Y.H. performed experiments. Y.Z. analyzed the results with the assistance of M.Q. wrote the first manuscript and revised by S.X. supervised the project. C.X. and Y.Z. contributes the performance comparison.

Declarations

Competing interests

The authors declare no competing interests.

Additional information

Correspondence and requests for materials should be addressed to S.X.

Reprints and permissions information is available at www.nature.com/reprints.

Publisher's note Springer Nature remains neutral with regard to jurisdictional claims in published maps and institutional affiliations.

Open Access This article is licensed under a Creative Commons Attribution-NonCommercial-NoDerivatives 4.0 International License, which permits any non-commercial use, sharing, distribution and reproduction in any medium or format, as long as you give appropriate credit to the original author(s) and the source, provide a link to the Creative Commons licence, and indicate if you modified the licensed material. You do not have permission under this licence to share adapted material derived from this article or parts of it. The images or other third party material in this article are included in the article's Creative Commons licence, unless indicated otherwise in a credit line to the material. If material is not included in the article's Creative Commons licence and your intended use is not permitted by statutory regulation or exceeds the permitted use, you will need to obtain permission directly from the copyright holder. To view a copy of this licence, visit http://creativecommons.org/licenses/by-nc-nd/4.0/.

© The Author(s) 2025